Draft version November 22, 2016
Preprint typeset using LaTeX style emulateapj v. 5/2/11

arXiv:1611.06489v1 [astro-ph.GA] 20 Nov 2016

NON-AXISYMMETRIC VERTICAL VELOCITY DISPERSION DISTRIBUTIONS PRODUCED BY BARS

Min Du[1, 2], Juntai Shen[1, 2], Victor P. Debattista[2, 3]

Draft version November 22, 2016

ABSTRACT

In barred galaxies, the contours of stellar velocity dispersions (σ) are generally expected to be oval and aligned with the orientation of bars. However, many double-barred (S2B) galaxies exhibit distinct σ peaks on the minor axis of inner bar, which we termed "σ-humps," while two local σ minima are present close to the ends of inner bars, i.e., "σ-hollows." Analysis of numerical simulations shows that σ_z-humps or hollows should play an important role in generating the observed σ-humps+hollows in low-inclination galaxies. In order to systematically investigate the properties of σ_z in barred galaxies, we apply the vertical Jeans equation to a group of well-designed three-dimensional bar+disk(+bulge) models. A vertically thin bar can lower σ_z along the bar and enhance it perpendicular to the bar, thus generating σ_z-humps+hollows. Such a result suggests that σ_z-humps+hollows can be generated by the purely dynamical response of stars in the presence of a, sufficiently massive, vertically thin bar, even without an outer bar. Using self-consistent N-body simulations, we verify the existence of vertically thin bars in the nuclear-barred and S2B models which generate prominent σ-humps+hollows. Thus the ubiquitous presence of σ-humps+hollows in S2Bs implies that inner bars are vertically thin. The addition of a bulge makes the σ_z-humps more ambiguous and thus tends to somewhat hide the σ_z-humps+hollows. We show that σ_z may be used as a kinematic diagnostic of stellar components that have different thickness, providing a direct perspective on the morphology and thickness of nearly face-on bars and bulges with integral-field unit spectroscopy.

Subject headings: galaxies: kinematics and dynamics — galaxies: structure — galaxies: stellar content — galaxies: bulges

1. INTRODUCTION

Near-infrared imaging surveys have shown that bars are ubiquitous stellar structures; in the local Universe about two-thirds of disk galaxies host elongated stellar bars (Eskridge et al. 2000; Whyte et al. 2002; Laurikainen et al. 2004a; Menéndez-Delmestre et al. 2007; Marinova & Jogee 2007). The fraction is $0.25 - 0.3$ if only strong bars are counted (e.g. Nilson 1973; de Vaucouleurs et al. 1991). From N-body simulations it is well known that bars can spontaneously form in galactic disks if the disk dynamical temperature (Toomre-Q) is not too high (e.g. Miller et al. 1970; Hohl 1971; Ostriker & Peebles 1973; Sellwood 1980, 1981; Athanassoula & Sellwood 1986a). Once formed bars are expected to be long-lived and difficult to destroy (Shen & Sellwood 2004; Debattista et al. 2006; Villa-Vargas et al. 2010; Athanassoula et al. 2013), which is supported by the fact that bars are typically composed of old stars (Gadotti & de Souza 2006; Sánchez-Blázquez et al. 2011). Observations of intermediate-redshift galaxies have revealed that the fraction of bars increases from $\sim 20\%$ at $z \sim 0.84$ to $\sim 65\%$ in the local Universe (Sheth et al. 2008). As the frequency of violent interactions between galaxies decreases, the evolution of galaxies is driven mainly by internal processes, so-called secular evolution. Galactic bars are the most important driver of the secular evolution of disk galaxies (see the reviews of Kormendy & Kennicutt 2004; Kormendy 2013). By transferring angular momenta to the outer disk and dark matter halo, bars may grow longer and stronger, but rotate slower (Debattista & Sellwood 1998, 2000; Athanassoula 2003). Bars can drive the transport and accumulation of gas toward galactic central regions, thus triggering nuclear starbursts and, possibly, fuelling active galactic nuclei (AGN) (e.g. Shlosman et al. 1989, 1990; Buta & Combes 1996; Bournaud & Combes 2002; Maciejewski 2004a,b; García-Burillo et al. 2005; Hopkins & Quataert 2010; Kim et al. 2012; Emsellem et al. 2015; Li et al. 2015). Numerical simulations also suggest that bar formation can trigger the vertical buckling instability, leading to boxy/peanut (B/P) bulges (Raha et al. 1991; Merritt & Sellwood 1994).

Being composed primarily of old stars, bars can be traced well in infrared bands where the dust extinction is much weaker than that in visible bands. The morphology of bars have been systematically investigated through ellipse fitting and Fourier decomposition of infrared images (e.g. Chapelon et al. 1999; Knapen et al. 2000; Laine et al. 2002; Laurikainen & Salo 2002; Laurikainen et al. 2002; Erwin 2005). Early dynamical studies of bars used long-slit spectroscopy of stars and ionized gas (e.g. Kuijken & Merrifield 1995; Bureau & Freeman 1999; Vega Beltrán et al. 2001). In the last decade, the development of integral-field unit (IFU) spectroscopy has made it possible to study the 2D kinematics of nearby galaxies. The kinematics of disks and bars have been quantified in several IFU surveys, e.g. SAURON (de Zeeuw et al. 2002), ATLAS^{3D} (Cappellari et al. 2011), CALIFA (Sánchez et al. 2012), DiskMass (Bershady et al. 2010),

[1] Key Laboratory of Research in Galaxies and Cosmology, Shanghai Astronomical Observatory, Chinese Academy of Sciences, 80 Nandan Road, Shanghai 200030, China
[2] Correspondence should be addressed to dumin@shao.ac.cn; jshen@shao.ac.cn; VPDebattista@uclan.ac.uk
[3] Jeremiah Horrocks Institute, University of Central Lancashire, Preston, PR1 2HE, UK

and MaNGA (Bundy et al. 2015) (see review by Cappellari 2016). However, knowledge of the kinematic properties of bars is still incomplete. In early-type barred galaxies the central kinematic major axis is misaligned from the line of nodes (LON) by around $\sim 5^\circ$ (Cappellari et al. 2007; Krajnović et al. 2011). This is probably because the elongated streaming motions in bars distort the velocity fields, as shown in numerical studies (Miller & Smith 1979; Vauterin & Dejonghe 1997; Bureau & Athanassoula 2005). According to N-body simulations, the kinematic misalignment is not prominent in bars of early-type galaxies, possibly, because large random motions dominate (Du et al. 2016). Generally, face-on or moderately inclined bars are expected to generate oval velocity dispersion (σ) contours aligned with the bar (Debattista et al. 2005; Iannuzzi & Athanassoula 2015; Du et al. 2016).

The most surprising σ features are the σ-humps and hollows found in double-barred (S2B) galaxies. Using SAURON IFU spectroscopy, de Lorenzo-Cáceres et al. (2008) found that the σ maps of S2Bs reveal two local minima at the ends of inner bars, which they termed "σ-hollows." Du et al. (2016) showed that such σ-hollows can be reproduced in the self-consistent simulations of S2Bs, which match well the σ features in the S2Bs in the ATLAS^{3D} and SAURON surveys. The S2B simulations exhibit double-peaked σ enhancements along the minor axis of inner bars as well, termed "σ-humps," which are also seen in the observations. Optical and near-infrared observations have revealed that multi-bar structures are quite common in the local Universe; almost one-third of early-type barred galaxies host S2B structures (Erwin & Sparke 2002; Laine et al. 2002; Erwin 2004). Many observations have shown that in S2Bs small-scale inner bars are dynamically decoupled from their large-scale outer counterparts (Buta & Crocker 1993; Friedli & Martinet 1993; Corsini et al. 2003). Inner bars are generally expected to rotate faster than outer ones. The physical origin of σ-humps+hollows is still unclear. Du et al. (2016) reported that σ-humps+hollows often accompanied nuclear bars in single-barred models. Therefore, σ-humps+hollows are not unique features of S2Bs, and cannot arise from the interaction of two bars. de Lorenzo-Cáceres et al. (2008) proposed that σ-hollows are simply caused by the contrast of a dynamically cold inner bar embedded in a relatively hotter bulge. In Du et al. (2016) we compared the difference in intrinsic kinematics between the model with σ-humps+hollows to that without σ-humps+hollows. Their only difference is the double-peaked vertical velocity dispersion (σ_z) enhancements perpendicular to the inner bar, i.e., σ_z-humps, which must play an important role in generating σ-humps+hollows.

In this paper, we investigate the σ_z properties in a family of analytical models of barred galaxies, i.e., bar+disk systems, which are introduced in Section 2. The analytical results are presented in Section 3, where we successfully explain the physical origin of σ_z-humps+hollows from a purely dynamical point of view. In Section 4, we test the effect of a massive bulge component on σ_z features. In Section 5, using the self-consistent nuclear-barred and large-scale single-barred simulations, we verify the analytical results. We further demonstrate that σ_z can be used as a kinematic diagnostic of the relative thickness of different stellar components. Finally, we summarize the conclusions of this work in Section 6.

2. METHOD

2.1. *Vertical Jeans equation*

Galactic disks are equilibrium systems whose stellar kinematics must satisfy the Jeans equations (Binney & Tremaine 2008, Equation 4.208) which were first applied to stellar systems by Jeans (1922). For disk galaxies, the Jeans equations generally cannot be uniquely solved in the disk plane (the $x-y$ plane in Cartesian coordinates) without assumptions. In this paper we are only concerned with the vertical Jeans equation, i.e., the z direction, which can be written as

$$\frac{\partial(\rho_\star \sigma_{xz}^2)}{\partial x}+\frac{\partial(\rho_\star \sigma_{yz}^2)}{\partial y}+\frac{\partial(\rho_\star \sigma_z^2)}{\partial z}=-\rho_\star\frac{\partial\Phi}{\partial z}=\rho_\star F_z, \quad (1)$$

where $\sigma_{iz}^2=\overline{v_i v_z}-\bar{v_i}\bar{v_z}=\overline{v_i v_z}$; $i=x,y,z$, assuming $\bar{v_z}$ is always zero. σ_{zz}^2 is written as σ_z^2 for short. F_z is the vertical gravitational force from the total potential (Φ) which includes the contributions from stars and the dark matter halo. $\rho_\star$ is the volume density of the stellar component. With the boundary condition $\rho_\star=0$ as $z\to\infty$, the integral from z to ∞ gives

$$\begin{aligned}\rho_\star(z)\sigma_z^2(z)=&-\int_z^\infty \rho_\star(z')F_z(z')\mathrm{d}z'\\&+\int_z^\infty\left[\frac{\partial(\rho_\star\sigma_{xz})}{\partial x}+\frac{\partial(\rho_\star\sigma_{yz})}{\partial y}\right]\mathrm{d}z'.\end{aligned} \quad (2)$$

Corresponding to the anisotropic pressure forces, the second-order velocity moments, σ_{xz} and σ_{yz}, are omitted in the following analyses, thus

$$\rho_\star(z)\sigma_z^2(z)\approx-\int_z^\infty\rho_\star(z')F_z(z')\mathrm{d}z'. \quad (3)$$

The legitimacy of this assumption in barred galaxies will be discussed in Section 5.1. The integral of the velocity dispersion in the face-on view is obtained by

$$\begin{aligned}\left\langle\sigma_z^2\right\rangle=\frac{\int_{-\infty}^{+\infty}\rho_\star\sigma_z^2\mathrm{d}z}{\int_{-\infty}^{+\infty}\rho_\star\mathrm{d}z}&=\frac{\int_{-\infty}^{+\infty}\rho_\star\sigma_z^2\mathrm{d}z}{\Sigma}\\&\approx\frac{-\int_{-\infty}^{+\infty}\int_z^\infty\rho_\star(z')F_z(z')\mathrm{d}z'\mathrm{d}z}{\Sigma}.\end{aligned} \quad (4)$$

Therefore, the vertical dynamics give a simple relation between the density distribution of stars and the vertical velocity dispersion σ_z. Assuming a reasonable vertical density distribution, the axisymmetric form of this relation has been used as a kinematic estimator of the stellar disk mass in DiskMass IFU survey (Bershady et al. 2010, 2011; Martinsson et al. 2013a,b; Angus et al. 2015). In the DiskMass survey, the influence of bars is generally ignored by selecting a sample of unbarred or small/weakly barred galaxies.

2.2. *Equilibrium bar+disk models*

A σ_z map for any arbitrary density distribution can be numerically computed using Eqn. 4. In order to study the σ_z features in barred galaxies, we use a family of bar+disk models that are embedded in a dark matter

TABLE 1
Settings of the bar+disk systems

Name	h_z	$M_{\rm B}$	Ferrers n	$a/b/c$
E0	0.3	0		
E1	0.3	0.01	1.0	1.0/0.4/0.1
E2	0.3	0.03	1.0	1.0/0.4/0.1
E3	0.3	0.05	1.0	1.0/0.4/0.1
L1	0.1	0.05	1.0	1.0/0.4/0.1
L2	0.2	0.05	1.0	1.0/0.4/0.1
E4	0.3	0.05	1.0	1.0/0.2/0.1
E5	0.3	0.05	1.0	1.0/0.6/0.1
E6	0.3	0.05	1.0	1.0/0.4/0.3
E7	0.3	0.05	1.0	1.0/0.4/0.5
E8	0.3	0.05	1.0	2.0/0.4/0.1
E9	0.3	0.20	1.0	2.0/0.4/0.1
E10	0.3	0.20	1.0	2.0/0.4/0.3

Note. — From left to right: model name, disk scaleheight h_z, bar mass $M_{\rm B}$, Ferrers n, and axial ratio of bars $a/b/c$.

potential. In cylindrical coordinates, the disk density we use is given by a simple double-exponential distribution

$$\rho_{\rm D}(R,z) = \frac{\Sigma_0}{2h_z}\exp(-\frac{R}{h_R}-\frac{z}{h_z}), \tag{5}$$

where Σ_0, h_R, and h_z are the central surface density, scalelength, and scaleheight, respectively, of the disk component. Thus the disk mass $M_{\rm D}$ is $2\pi\Sigma_0 h_R^2$. To simplify the following analyses, we use the same unit system as in Du et al. (2015), i.e., $M_{\rm D} = G = h_R = V_0 = 1$.

The bar component is modelled as a triaxial Ferrers ellipsoid (Ferrers 1877)

$$\rho_{\rm B}(x,y,z) = \begin{cases} \rho_{\rm B0}(1-m^2)^n & m \le 1 \\ 0 & m > 1, \end{cases} \tag{6}$$

where $m^2 = x^2/a^2 + y^2/b^2 + z^2/c^2$ in the Cartesian coordinate. The bar is aligned along the x-axis; the values of a, b, and c determine the semi-major axis, semi-minor axis, and thickness, respectively, of the bar. The axial ratio b/a corresponds to the ellipticity (ϵ) of the bar. The Ferrers n parameter determines how fast the density decreases outward. Photometric observations show that the typical density profiles of bars are shallow (flat) and clearly truncated in early-type galaxies, while in late-type galaxies they tend to decrease outward following a more exponential profile (Elmegreen & Elmegreen 1985; Chapelon et al. 1999; Laine et al. 2002; Laurikainen & Salo 2002; Laurikainen et al. 2002; Kim et al. 2016). The central density of the bar, $\rho_{\rm B0}$, is numerically calculated for a given total mass of the bar, $M_{\rm B}$. We use the same dark matter potential as in the N-body simulations of Du et al. (2015)

$$\Phi_{\rm DM} = \frac{1}{2}V_h^2\ln(r^2+r_h^2), \tag{7}$$

where $V_h = 0.6$ and $r_h = 15$.

In such bar+disk systems, there are six free parameters in total: the disk scaleheight h_z, bar mass $M_{\rm B}$, and four structural parameters of the bar a, b, c, and Ferrers n. The Ferrers n is fixed at 1.0 to generate a shallow bar model. Given a set of parameters, we use a $N_x \times N_y \times N_z = 201 \times 201 \times 401$ grid to calculate the gravitational potential of the total system with a parallel 3D Poisson solver PSPFFT (Budiardja & Cardall 2011). The model is located at the geometric center of the grid, and the spatial resolution is constant at 0.01 along the z direction as $z \in [-2.0, 2.0]$. Including the dark matter potential, we numerically compute σ_z using Eqn. 4.

Systematic studies of near-infrared images of barred galaxies have shown that the semi-major axis of bars varies up to $2.5h_R$, with the mean values $\sim 1.3h_R$ and $\sim 0.6h_R$ for early-type and late-type galaxies, respectively (Erwin 2005; Menéndez-Delmestre et al. 2007; Díaz-García et al. 2016). The scalelength of disk galaxies seems to be independent of their Hubble type (de Jong 1996; Graham & de Blok 2001; Fathi et al. 2010). However, optical and near-infrared observations of edge-on galaxies find a decreasing trend of the scaleheight h_z from early-type to late-type galaxies (de Grijs 1998; Schwarzkopf & Dettmar 2000; Bizyaev et al. 2014; Mosenkov et al. 2015).

Table 1 shows the set of parameters we choose to study the σ_z features of barred galaxies. According to the empirical relation of de Grijs (1998), the ratio h_R/h_z varies from $1-5$ (the median value ~ 4) in early-type spirals ($T \le 1$) to $5-12$ (the median value ~ 9) in very late-type spirals ($T \ge 5$). Thus we vary h_z from 0.3 to 0.1 in our analytical models. In the cases of $h_z = 0.3$, we name such early-type-like ("E") double-exponential models as "E*." The late-type-like double-exponential models are named as "L*" in the cases of $h_z = 0.1$ or 0.2. The model E0 is a purely axisymmetric disk without a bar, i.e., $M_{\rm B} = 0$. A typical bar is used in most models by setting $a = h_R = 1.0$ and $b/a = 0.4$. In the models E1-7 and L1-2 the bar length ($a = 1.0$) is half of that in E8-10 ($a = 2.0$). We truncate the disk at twice the bar length in order to reduce the calculation time, which allows us to obtain a high enough spatial resolution in the $x-y$ plane (0.02 in E0-7 and L1-2; 0.04 in E8-10). We have confirmed that using a larger truncation radius makes negligible difference in the σ_z map. The dark matter potential also has a tiny effect on σ_z.

To better understand the σ_z features, we further decompose the contributions of the bar and the disk components as follows

$$\left\langle\sigma_z^2\right\rangle = \frac{\Sigma_{\rm D}}{\Sigma_{\rm tot}}\left\langle\sigma_z^2\right\rangle_{\rm D} + \frac{\Sigma_{\rm B}}{\Sigma_{\rm tot}}\left\langle\sigma_z^2\right\rangle_{\rm B}, \tag{8}$$

where $\Sigma_{\rm D}$, $\Sigma_{\rm B}$, and $\Sigma_{\rm tot}$ are the surface density of the disk, bar, and total stellar system, respectively. $\langle\sigma_z\rangle_{\rm D}$ and $\langle\sigma_z\rangle_{\rm B}$ are the intrinsic vertical velocity dispersions of the disk and the bar, respectively. According to Eqn. 4, $\left\langle\sigma_z^2\right\rangle_{\rm D}$ and $\left\langle\sigma_z^2\right\rangle_{\rm B}$ can be calculated as

$$\begin{aligned} \left\langle\sigma_z^2\right\rangle_{\rm D} &= \frac{-\int_{-\infty}^{+\infty}\int_z^{\infty}\rho_{\rm D}F_z{\rm d}z'{\rm d}z}{\Sigma_{\rm D}} \\ \left\langle\sigma_z^2\right\rangle_{\rm B} &= \frac{-\int_{-\infty}^{+\infty}\int_z^{\infty}\rho_{\rm B}F_z{\rm d}z'{\rm d}z}{\Sigma_{\rm B}}, \end{aligned} \tag{9}$$

where F_z is the total vertical force. In following analyses, we weight the disk and the bar σ_z by the surface density, i.e., the disk $\sigma_z = \sqrt{\Sigma_{\rm D}\left\langle\sigma_z^2\right\rangle_{\rm D}/\Sigma_{\rm tot}}$ and the bar $\sigma_z = \sqrt{\Sigma_{\rm B}\left\langle\sigma_z^2\right\rangle_{\rm B}/\Sigma_{\rm tot}}$. Thus the disk and the bar σ_z are their respective contributions to the total σ_z. The bulge σ_z will be defined similarly when a bulge is added. As shown

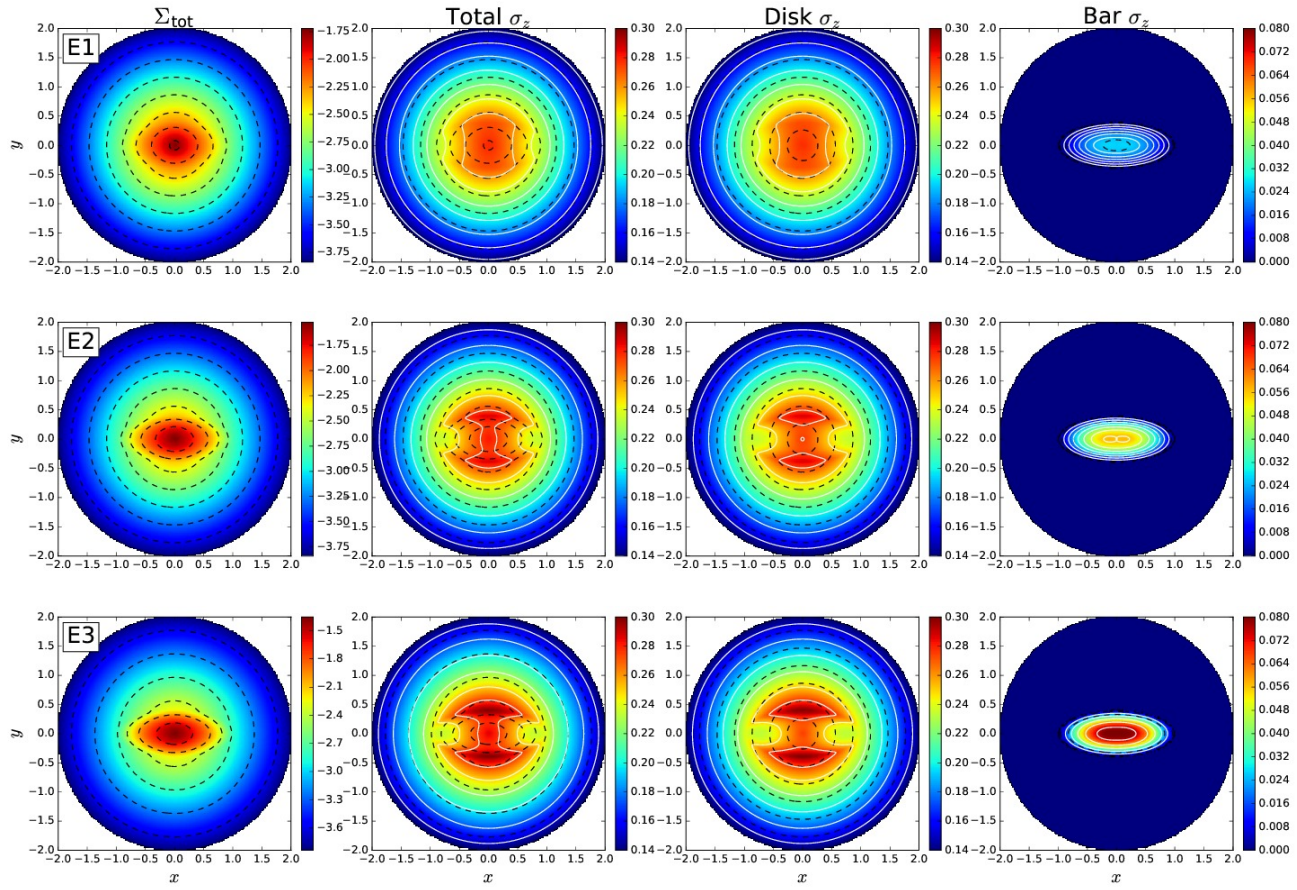

FIG. 1.— Total surface density $\Sigma_{\rm tot}$ and σ_z maps of the models E1-3 in Table 1, showing the variation of σ_z fields with increasing bar mass. From top to bottom, the bar mass is set to $0.01M_{\rm D}$ (E1), $0.03M_{\rm D}$ (E2), and $0.05M_{\rm D}$ (E3), respectively. From left to right: $\Sigma_{\rm tot}$, total σ_z, disk σ_z, and bar σ_z. The isodensity contours are equally separated in logarithmic space and σ_z contours of each map are overlaid using black dashed and white solid curves, respectively.

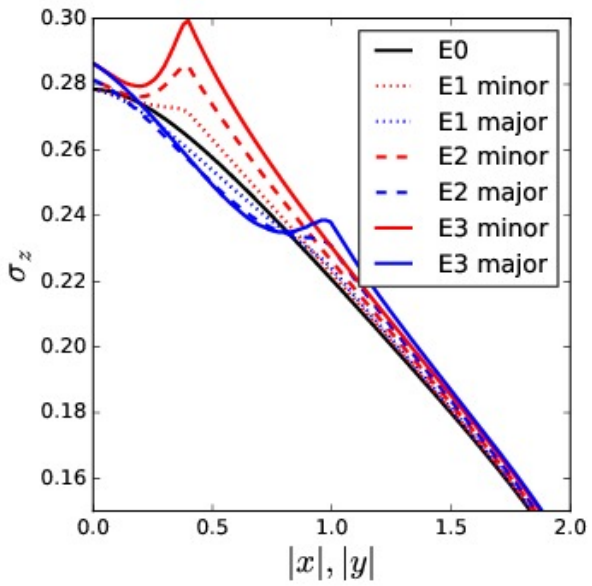

FIG. 2.— 1D σ_z profiles along the minor (red) and major (blue) axes of the bars in the models E0-3, varying the bar mass $M_{\rm B}$. The black solid profile in the left panel shows the σ_z profile of the pure-disk model E0.

in Table 1, we explore the effect of bar mass $M_{\rm B}$ (E0-3), ellipticity a/b (E3-5), thickness c (E3, E6-7), and semi-major axis a (E3, E8-10) of the Ferrers bar. E3 exhibits prominent σ-humps+hollows. The models L1-2 show the effect of disk scaleheight h_z.

3. ANALYTICAL RESULTS: THE σ_Z FEATURES IN BAR+DISK SYSTEMS

3.1. *Bar mass*

The pure-disk model, E0, generates an axisymmetric σ_z distribution as expected. Adding a bar and keeping its shape constant at $a/b/c = 1.0/0.4/0.1$, we increase the bar mass by varying $M_{\rm B}$ from $0.01M_{\rm D}$ in E1 to $0.05M_{\rm D}$ in E3. The total surface density $\Sigma_{\rm tot}$ (the first column) and resulting σ_z maps of E1-3 are shown in Fig. 1. The second column shows the total σ_z of the bar+disk systems. The disk and the bar σ_z, weighted by the respective surface density, are shown in the third and fourth columns, respectively. As the bar mass increases, we can see more prominent σ_z-humps+hollows along the minor/major-axis of the bar. In order to better appreciate the amplitudes of the σ_z-humps+hollows, we plot the 1D σ_z profiles along the minor (red) and major (blue) axes of the bars (Fig. 2). For comparison, the σ_z of E0 is overlaid in black. As shown in Fig. 2, E0-3 exhibit almost the same distribution of σ_z at large radii ($R > 1.2$), suggesting that the influence of the bar is

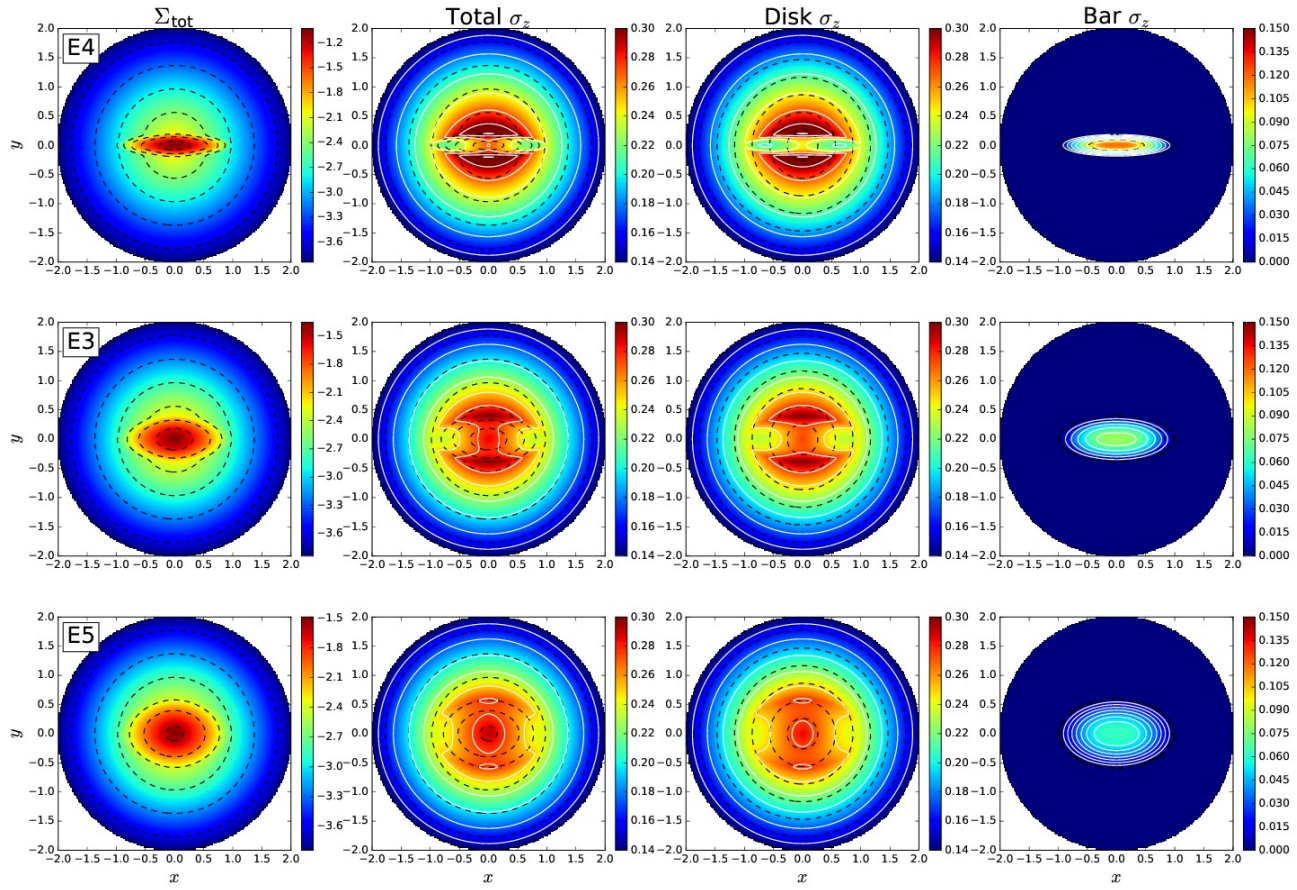

FIG. 3.— Models E4, E3, and E5 in Table 1, showing the variation of σ_z fields when varying the minor-to-major axial ratio b/a to 0.2 (E4), 0.4 (E3), and 0.6 (E5).

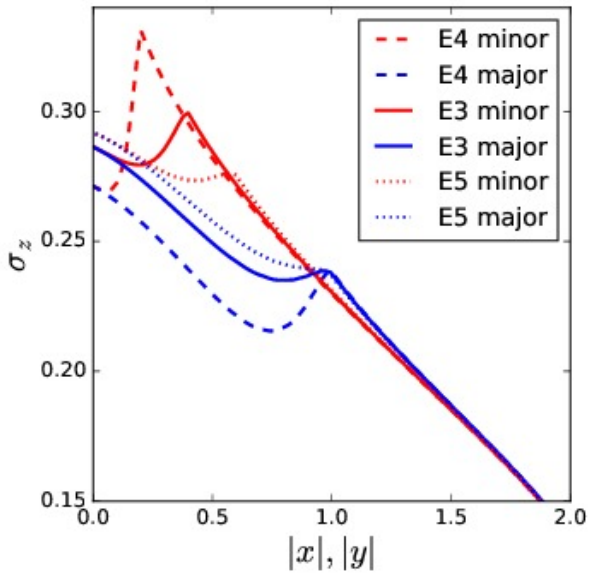

FIG. 4.— 1D σ_z profiles along the minor (red) and major (blue) axes of the bars in the models E4-3 and E5, varying the minor-to-major axial ratio b/a of the bar.

important only in the inner region, where it dominates. With the bar mass increasing, in E2-3 the σ_z values are significantly enhanced on the minor axis of the bar, i.e., σ_z-humps form, which are clearly induced by the non-axisymmetric bar potential. In contrast, σ_z values are reduced along the major axis of the bar, thus forming σ_z-hollows. As shown in Fig. 1, the disk σ_z maps (the third column) also show σ_z-humps+hollows as in the total σ_z maps, while none are present in the bar σ_z (the fourth column). The oval σ_z contours of the bar are aligned with the bar. Therefore, surprisingly, although the σ_z-humps are supported by the bar potential, they are mainly present in the disk component, extending beyond the bar along the minor axis. This result is consistent with observations (de Lorenzo-Cáceres et al. 2008; Du et al. 2016) and simulations (Du et al. 2016) of S2Bs.

3.2. *Bar ellipticity and thickness*

In the analysis above, we have shown that even a relatively lightweight bar ($0.05M_{\rm D}$) can generate prominent σ_z-humps+hollows. However, in most IFU observations and N-body simulations of barred galaxies, bars do not usually generate σ_z-humps+hollows. Currently, σ-humps+hollows have been seen only in the cases of S2Bs. In order to identify the condition for generating σ_z-humps+hollows, we study the effect of bar properties (a, b, and c) on σ_z. As shown in Table 1, fixing $a = 1.0$, we vary b and c in models E3-7. The bar ellipticity is varied from 0.8 ($b/a = 0.2$) in E4 to 0.4 ($b/a = 0.6$) in E5 (Fig. 3). The variation of the 1D profiles of σ_z-humps+hollows is shown in Fig. 4. Here the thickness of the bars is fixed at $c = 0.1$, i.e., a vertically thin bar. It is clear that a larger ellipticity, i.e., smaller

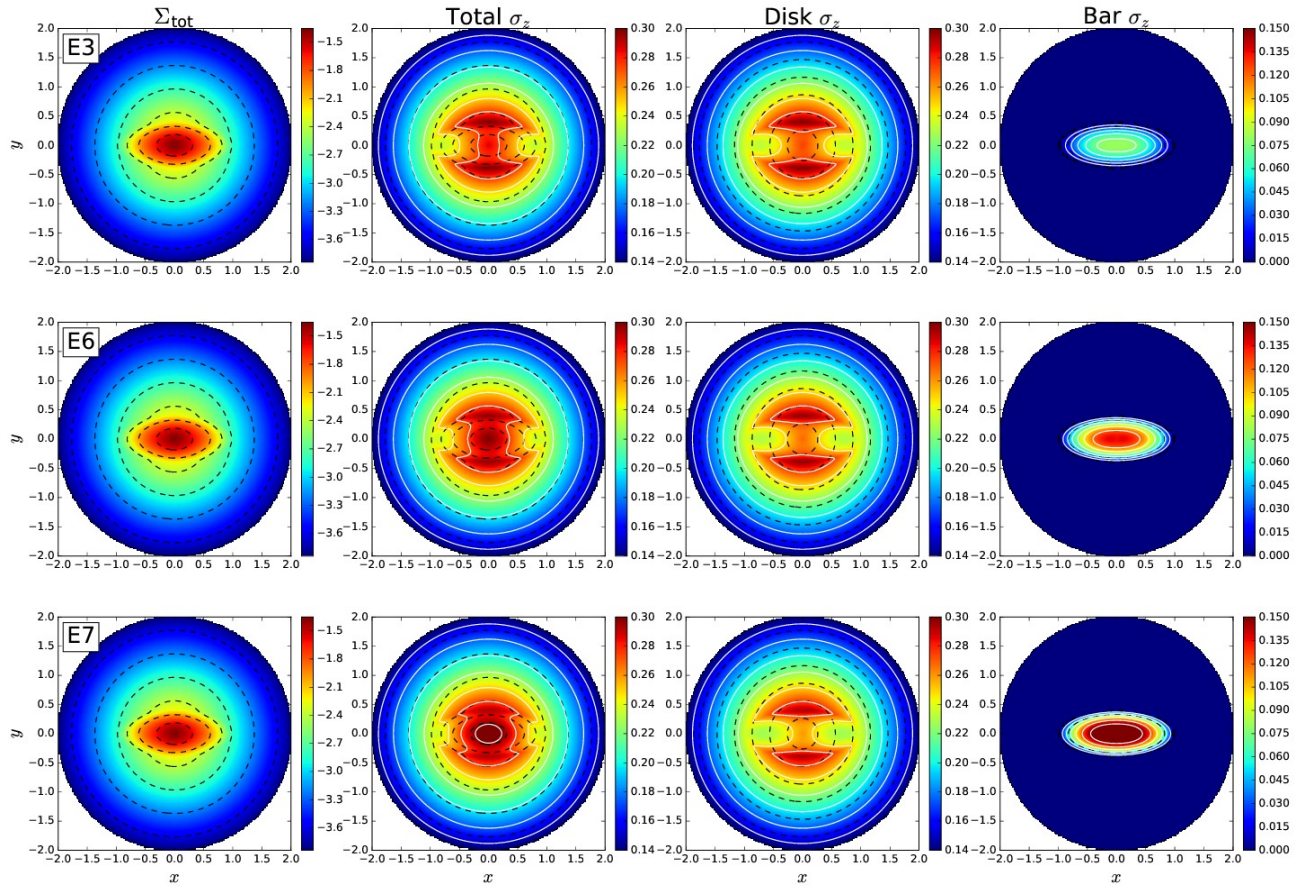

FIG. 5.— Models E3, E6, and E7 in Table 1, showing the variation of σ_z fields with varying bar thickness c from 0.1 in E3 to 0.5 in E7.

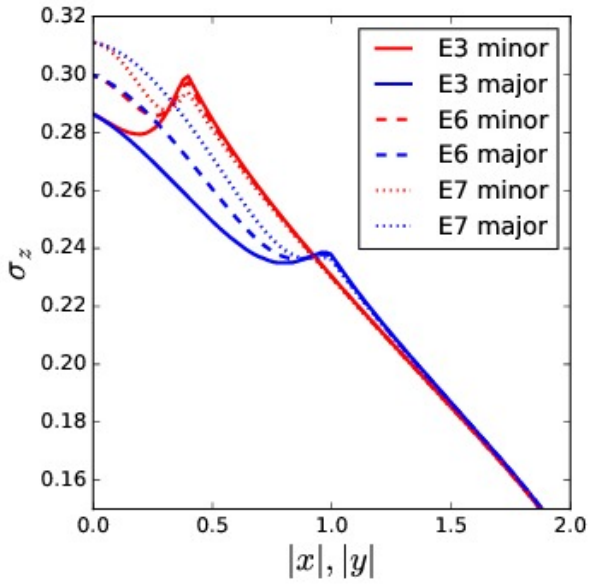

FIG. 6.— 1D σ_z profiles along the minor (red) and major (blue) axes of the bars in the models E3 and E6-7, varying the thickness c of the bar.

b/a, generates more prominent σ_z-humps as well as hollows.

In models E3 and E6-7 we vary the bar thickness from 0.1 in E3 to 0.5 in E7 using a constant $b/a = 0.4$ (Fig. 5). As shown in Fig. 6, the central σ_z-drop gradually becomes a σ_z-peak as the bar thickness increases. Because of the enhancement of the bar σ_z (the fourth column of Fig. 5), the σ_z-humps+hollows become less prominent when the bar is thick. The disk σ_z is almost unchanged with increasing bar thickness (the third column). As a result, the total σ_z contours of E7 are oval and aligned with the bar.

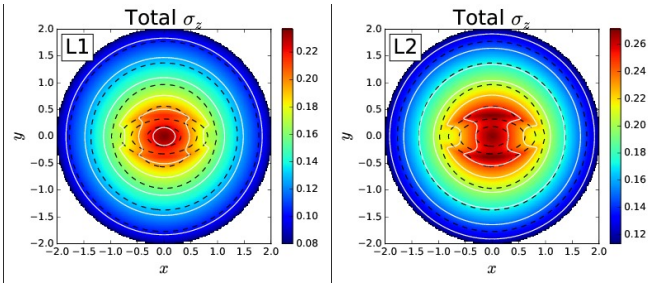

FIG. 7.— Total σ_z maps of the models L1-2. The disk scale-height h_z varies from 0.1 in L1 to 0.2 in L2. The overlaid black dashed and white solid curves show the isodensity and σ_z contours, respectively.

In Fig. 7 we show the total σ_z maps of the late-type-like models L1-2. Using a vertically thinner disk in L1 ($h_z = 0.1$) and L2 ($h_z = 0.2$), σ_z is reduced. There are no prominent σ_z-humps+hollows present in L1. Thus a vertically even thinner bar is required to generate σ_z-humps+hollows in late-type galaxies which are expected to be thinner than early-type galaxies.

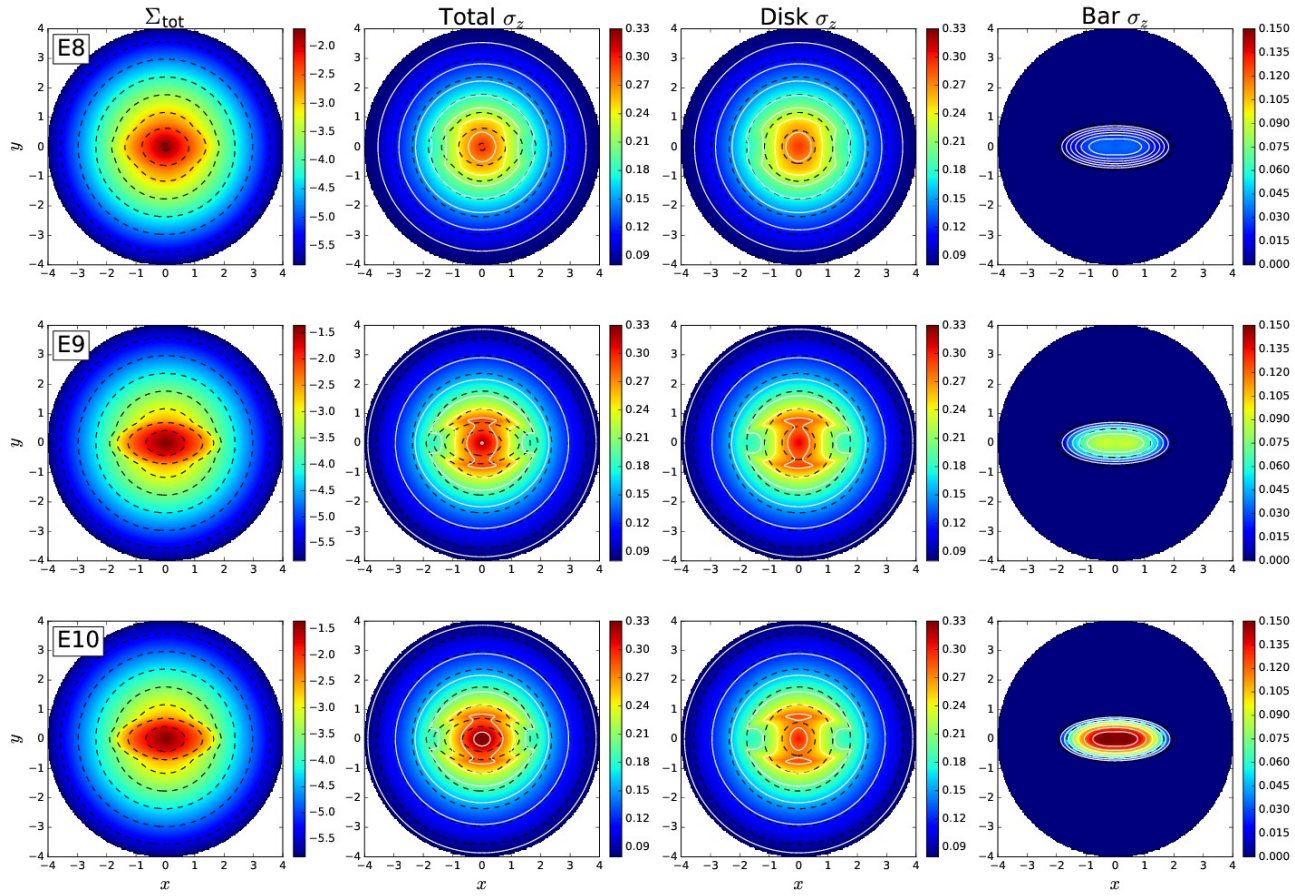

FIG. 8.— Models E8-10 in Table 1, showing the σ_z maps of the long bar+disk models. The bar is twice the size of the bars in E1-7, i.e., $a = 2.0, b = 0.8$. The bar mass in E8-10 is $0.05M_{\rm D}, 0.2M_{\rm D}$, and $0.2M_{\rm D}$, respectively. The bars in E8-9 ($c = 0.1$) are vertically thinner than the one in E10 ($c = 0.3$).

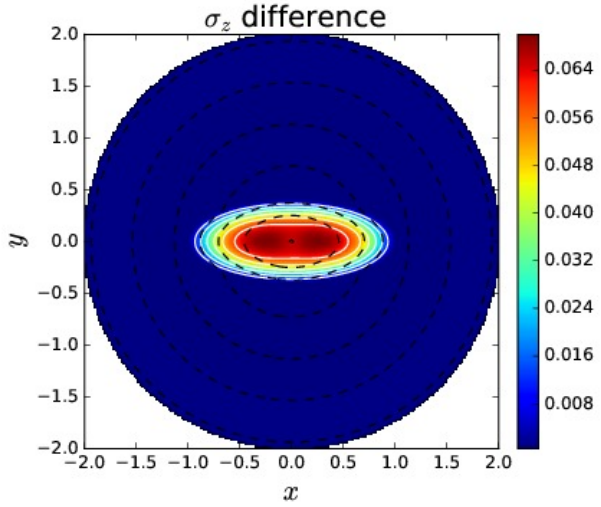

FIG. 9.— Map of the σ_z difference, obtained by subtracting the total σ_z field of E3 from that of the model using a vertically exponential density profile with a constant $h_{Bz} = h_z = 0.3$. The overlaid black dashed and white solid curves show the isodensity and σ_z difference contours, respectively.

3.3. *Bar length*

Using the models E1-7, we have studied the conditions for generating σ_z-humps+hollows in galaxies hosting a typical bar of length $a = 1.0$. We further examine the σ_z features in the long bar+disk models E8-10 using $a = 2.0, b = 0.8$ (Table 1). The bar in E8 has the same mass ($0.05M_{\rm D}$) and thickness ($c = 0.1$) as E3, thus the size increase makes the bar potential shallower. As shown in the first row of Fig. 8, E8 generates quite round σ_z contours as the shallow bar potential supports only weak non-axisymmetric σ_z features. We set a more massive bar of mass $0.2M_{\rm D}$ in E9-10, varying c from 0.1 in E9 to 0.3 in E10. As shown in Fig. 8, there are no prominent σ_z-humps+hollows present in E9-10, although the moderately enhanced σ_z patterns are somewhat rectangular shaped in their outer parts. Such a result suggests that it is more difficult to generate central σ_z-humps+hollows in long bars than in short ones. Compared to E3, E9 has a similar bar σ_z distribution, but its disk σ_z is much larger at the center as a result of shallower potential.

3.4. *Vertical density distribution of bars*

According to the analyses above, σ_z-humps+hollows are primarily generated by the dynamical response of stars to the potential of a vertically thin, sufficiently massive, and relatively short bar. In photometric observations, we can easily measure the length, ellipticity, and mass of bars, especially in low-inclination galaxies, whereas we know little about their vertical density distributions. Although numerical simulations have been widely used to study the 3D morphology and orbital structure of bars (Pfenniger 1984; Martinet & de Zeeuw

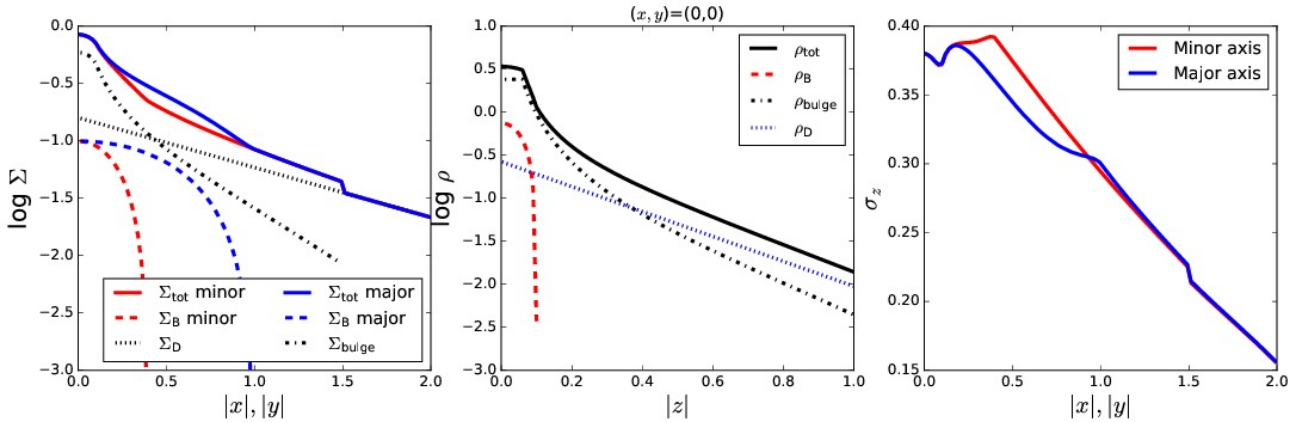

FIG. 10.— Model E3B, which is identical to the E3 model but with the addition of a bulge of mass $M_{\rm bulge} = 0.30M_{\rm D}$. In the left panel, we plot the logarithmic surface density profiles of the total system ($\Sigma_{\rm tot}$), bar ($\Sigma_{\rm B}$), bulge ($\Sigma_{\rm bulge}$), and disk ($\Sigma_{\rm D}$), where the red and the blue profiles correspond to the minor and the major axes, respectively. The middle panel shows the logarithmic vertical density distributions of the total system ($\rho_{\rm tot}$), bar ($\rho_{\rm B}$), bulge ($\rho_{\rm bulge}$), and disk ($\rho_{\rm D}$) at the center $(x, y) = (0, 0)$. The right panel shows the total σ_z profiles along the minor (red) and major (blue) axes of the bar.

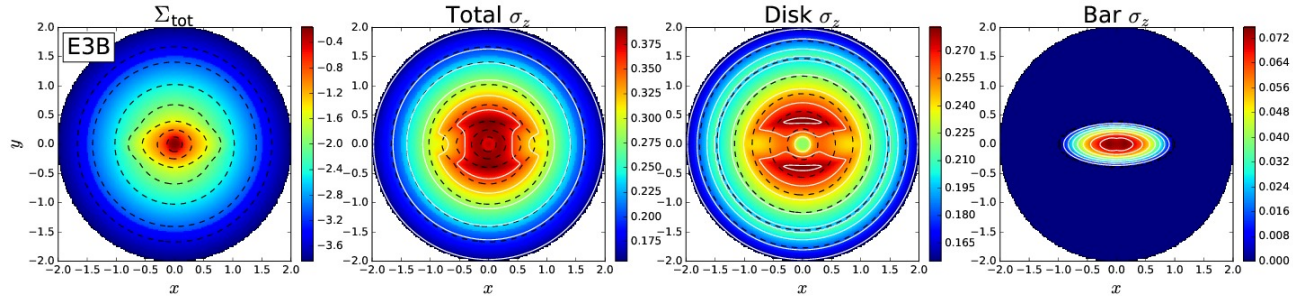

FIG. 11.— 2D $\Sigma_{\rm tot}$ and σ_z maps of E3B (Fig. 10).

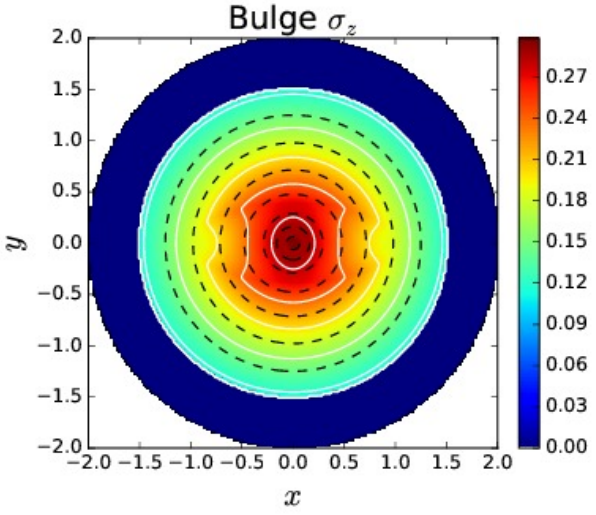

FIG. 12.— Bulge σ_z, weighted by the bulge surface density, i.e., $\sqrt{\Sigma_{\rm bulge}\langle\sigma_z^2\rangle_{\rm bulge}/\Sigma_{\rm tot}}$, of the model E3B. The overlaid black dashed and white solid curves show the isodensity and σ_z contours, respectively, of the bulge component.

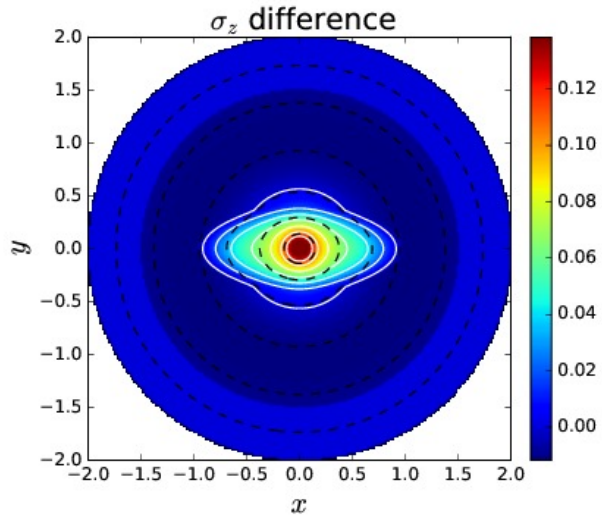

FIG. 13.— Map of the σ_z difference, obtained by subtracting the σ_z field of the model E3B from that of the model using the constant scaleheight 0.3. The overlaid black dashed and white solid curves show the isodensity and σ_z difference contours, respectively.

1988; Pfenniger & Friedli 1991; Sellwood & Wilkinson 1993; Skokos et al. 2002a,b; Patsis et al. 2003, 2002; Harsoula & Kalapotharakos 2009; Valluri et al. 2016), such theoretical models remain poorly tested by observations. We find that the bar σ_z is largely determined by the bar thickness, while the σ_z-humps arising in disks seem to be insensitive to its properties. It suggests that σ_z can be used as a tracer of the bar thickness. However, our assumption of the vertical density distribution on bars is still questionable. The exponential ($\rho(z) \propto \exp(-z/h_{Bz})$) and isothermal ($\rho(z) \propto \mathrm{sech}^2(z/2h_{Bz})$) profiles have also been widely used to approximate the vertical density distribution of real bars for the purpose

of estimating the bar strength (Buta & Block 2001; Laurikainen & Salo 2002; Laurikainen et al. 2004a,b, 2005; Salo et al. 2015; Díaz-García et al. 2016). In this paper we considered only models using Ferrers bars. But we have verified that a much thinner bar is also required to generate prominent σ_z-humps+hollows for a typical bar with vertically exponential or isothermal density profiles. In Fig. 9 the σ_z difference is obtained by subtracting the total σ_z of E3 from that of the model using a vertically exponential bar whose scaleheight is the same as the disk, i.e., $h_{Bz} = h_z = 0.3$. This helps to quantify how the variation of vertical density distribution of bars affects σ_z. As the difference in the total σ_z is almost only caused by the difference in the bar σ_z, the positive σ_z difference closely traces the thin bar in E3. The σ_z difference outside of the bar is close to zero. Thus the σ_z difference may be used as a diagnostic of the relative thickness of bars and their host disks.

4. THE EFFECT OF BULGES

In early-type disk galaxies, a large fraction of the luminosity comes from a massive spheroidal bulge. Having large random motions, bulges may affect the σ_z features significantly where σ_z-humps+hollows arise. In order to study the effect of a bulge on σ_z, we add an oblate, spheroidal power-law bulge in E3 using Eqn. 2.207 of Binney & Tremaine (2008)

$$\rho_{\rm bulge}(R,z) = \rho_{\rm b0} m^{-\alpha_b} e^{-m^2/r_b^2} \quad (R \le r_b), \qquad (10)$$

where $m = \sqrt{R^2 + z^2/q_b^2} \ge 0.1$. We set $\alpha_b = 1.8$ and $q_b = 0.6$ (Binney & Merrifield 1998, Section 10.2.1). In order to avoid the singularity at the center, $\rho_{\rm bulge}$ is set to be constant at $m \le 0.1$. The bulge is truncated at $r_b = 1.5$, so the bar is fully embedded in the bulge. The bulge mass is set to $0.3M_{\rm D}$. This bar+disk+bulge system is named as E3B. Along the minor and major axes of the bar, the profiles of the surface density and σ_z are shown in the left and the right panels, respectively, of Fig. 10. The vertical density profiles at the center are shown in the middle panel. It can clearly be seen that the bulge is more massive than the bar at any position.

The 2D $\Sigma_{\rm tot}$ and σ_z maps are shown in Fig. 11. As shown in the total σ_z map, the presence of the bulge significantly raise σ_z in the bulge region. It generates similar σ_z-humps along the minor axis to the simulations in Du et al. (2016), where the central σ_z-drop becomes more flat-topped (the right-most panel of Fig. 10) than E3. In the bulge (Fig. 12) the central σ_z contours are slightly oval and perpendicular to the bar. Such a result suggests that, in the bar potential the bulge component is not as responsive as the disk component, thus generating weaker non-axisymmetric σ_z features. The main influence of the bulge is to make the σ_z-humps less obvious by enhancing the central σ_z, thus hiding the σ_z-humps+hollows to a certain degree. By varying the thickness of the bar in such bar+disk+bulge systems (not shown here), we verify again that the bar needs to be much thinner than its host disk in order to generate visible σ_z-humps+hollows.

As presented in Section 3.4, the positive σ_z difference can be used as a tracer of the thin bar. As shown in Fig. 13, we obtain the σ_z difference of E3B using the same approach. We firstly regenerate the vertical density distribution of the whole system with the exponential function using a constant scaleheight 0.3, which is used to recalculate σ_z. Then the original σ_z field is subtracted from the recalculated σ_z. Outside the bulge the σ_z difference is close to zero; the regions having positive and negative σ_z difference trace well the intrinsic face-on morphology of the thin bar and thick bulge, respectively. Debattista et al. (2005) showed that the fourth-order Gauss-Hermite moment h_4 can be used as a kinematic diagnostic for bulges in nearly face-on galaxies. Here we show that σ_z differnce can be used as an alternative kinematic diagnostic of the stellar components having different thickness, e.g. thin bars and thick bulges, in barred galaxies.

5. *N*-BODY SIMULATIONS OF NUCLEAR AND LARGE-SCALE BARS

Using the bar+disk(+bulge) models, we have demonstrated that a vertically thin bar is required to generate σ_z-humps+hollows in barred galaxies. Such models allow us to study the effect of any single parameter by fixing the others. However, it is difficult to measure the 3D density distribution, especially perpendicular to the disk plane, in real galaxies. In order to verify the analytical results above, we study the 3D density distribution of self-consistent N-body simulations from Du et al. (2015, 2016). The unique advantage of simulations is that the 3D density distribution is completely known.

As shown in Fig. 14, we have studied two representative cases, namely, a nuclear-barred simulation "NB" (the top row) and a large-scale single-barred simulation "SB" (the bottom row). Here we briefly summarize the properties of the NB and the SB models (see more details in Du et al. 2015). Starting from a pure exponential disk with 4 million particles, the models were evolved using a 3D cylindrical polar grid code, `GALAXY` (Sellwood & Valluri 1997; Sellwood 2014). The unit system of the simulations is the same as the analytical models in Section 3. By reducing the Toomre-Q in the inner region, the initial inner disk generally triggers a significant nuclear bar instability, forming nuclear-barred galaxy or double-barred galaxy (Fig. 1 in Du et al. 2015). Possibly because of the heating of spirals driven by the nuclear bar, the outer disk in the NB model becomes too hot to form a bar (Athanassoula & Sellwood 1986b; Du et al. 2015). After reaching a quasi-steady state, the semi-major axis of the nuclear bar extends to ~ 0.7 of the initial h_R, making it a quite short bar. The NB model exhibits similar σ-humps+hollows as the standard S2B (Du et al. 2015, 2016). Thus the outer bar is not a necessary condition for generating σ-humps+hollows. It is worth emphasizing that the initial thickness of the NB model is smoothly lowered to 0.05 inside $R < 1.0$ from 0.1 in the outer region. In this case the NB model generates more prominent σ-humps+hollows (the top-left panel of Fig. 14) than the cases of using a radially constant thickness of 0.1.

Using a dynamically hotter initial inner disk normally leads to a large-scale single bar. The SB model here is exactly the same model as in Fig. 6 of Du et al. (2016) where the σ_z contours are oval and aligned with the bar (the bottom-left panel of Fig. 14). The semi-major axis of the bar in the SB model is ~ 3.0. Both the NB and the SB models are thickened in their inner regions ($R \sim 1.5$),

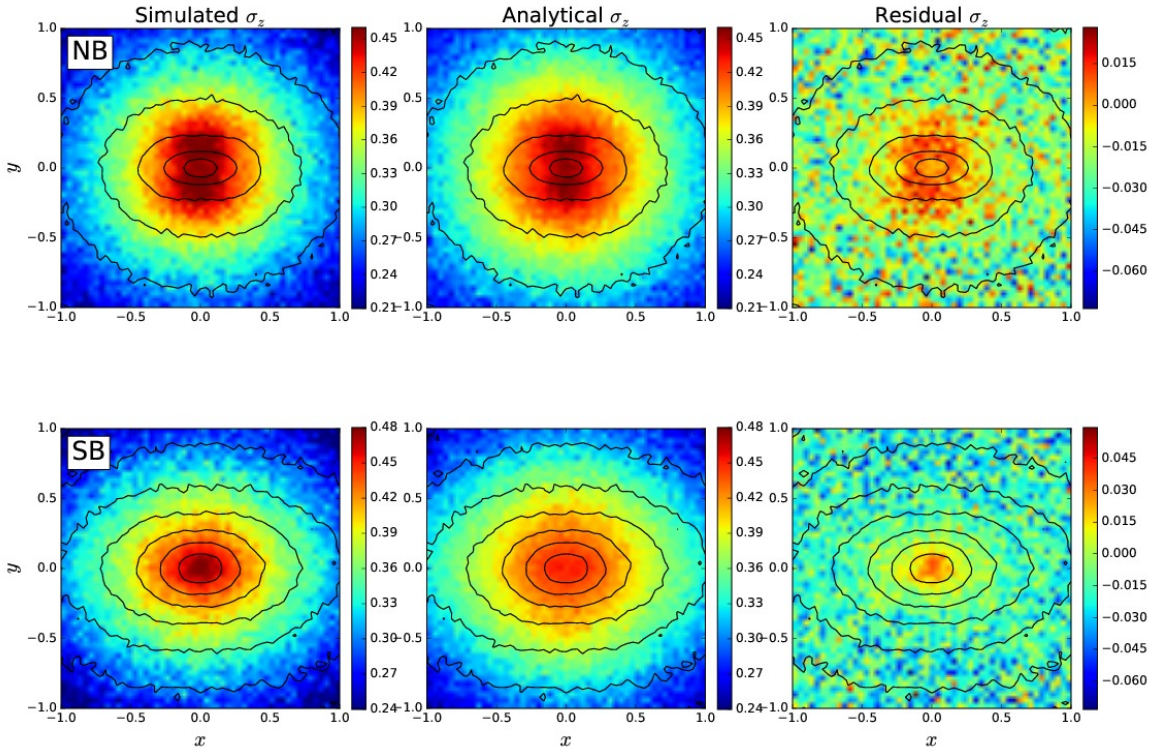

FIG. 14.— Maps of the simulated σ_z (left) and the analytical σ_z (middle) calculated using Eqn. 4, and the residual σ_z (right) of the nuclear-barred (NB, top) and the large-scale single-barred (SB, bottom) models. The residual σ_z, obtained by subtracting the analytical σ_z from the simulated σ_z, corresponds to the contribution of the anisotropic pressure in the simulations. We fix the color-bars of the left and middle columns. A much smaller range is used in the right column, as the maximum residual σ_z is at $\sim 5-10\%$ level of the simulated σ_z. The surface density contours are overlaid in black, separated in equal intervals in logarithmic space.

where boxy/peanut (B/P) bulges possibly form as seen from the edge-on view. Thus in the NB model the nuclear bar is embedded in the host bulge.

5.1. *Quantifying the uncertainty due to the anisotropic pressure in barred galaxies*

In this study we have assumed the velocity cross-terms are unimportant in the vertical dynamics (see Section 2.1), which is generally considered to be a good approximation in axisymmetric systems. However, this assumption is not obviously justified for non-axisymmetric bars which induce large streaming motions, possibly causing a systematic error in the σ_z calculation. In order to quantify the anisotropic pressure caused by the velocity cross-terms, we apply the vertical kinematic estimation to the NB and SB models. The density distribution and associated vertical force from the simulations are used to calculate the analytical σ_z (the middle column of Fig. 14). By subtracting the analytical σ_z from the simulation's actual σ_z (the left column), we obtain the residual σ_z (the right column) that corresponds to the contribution of the anisotropic pressure. We have confirmed that the residual σ_z here is well consistent with the numerically calculated anisotropic pressure.

The residual σ_z is roughly equal to zero all over the disk for the SB model. Only in the very central region is the residual σ_z positive at $\sim 10\%$ level, which has no effect on σ_z-humps+hollows. In the NB model there is an extensive positive residual σ_z ($\sim 5\%$ level) along the minor axis of the bar, which is possibly related to the elongated streaming motions in the nuclear bar. We have checked the standard S2B model as well, in which the anisotropic pressure enhances σ_z values along the minor axis of the inner bar at a similarly low level as the NB model. The maximum ellipticity of the simulated bars here reaches ~ 0.6. In observations some late-type bars can be very narrow and strong, in which case the importance of the anisotropic pressure may increase. Therefore, a cautious conclusion is that the anisotropic pressure is negligible in galaxies containing a normal or weak bar.

5.2. *A kinematic diagnostic of vertical thickness: σ_z*

As the anisotropic pressure is negligible, the σ_z features of the NB and SB models are mainly determined by their 3D density distributions and associated potentials. In this section, we investigate whether a vertically thin bar exists in the NB model, which our analysis in Section 3 suggests is a necessary condition for generating σ_z-humps+hollows (Fig. 15 and 16). The SB model is shown for comparison purpose.

In order to reduce the noise, we select the painted regions (annuli and filled dots in the left column of Fig. 15) to average the vertical density distribution. In both the NB (top) and SB (bottom) models the filled dots correspond to the minor axis (green), major axis (magenta), and center (black) of their bars. The cyan (at $R = 1.0$) and the red (at $R = 3.0$) annuli represent the B/P bulge and the outer disk regions, respectively. The red outer disk annulus in the NB model is not shown, as the computed region at $R = 3.0$ is beyond the boundary $[-2.0, 2.0]$ of the image. In Fig. 16 the average density distributions of each of these regions are indicated by

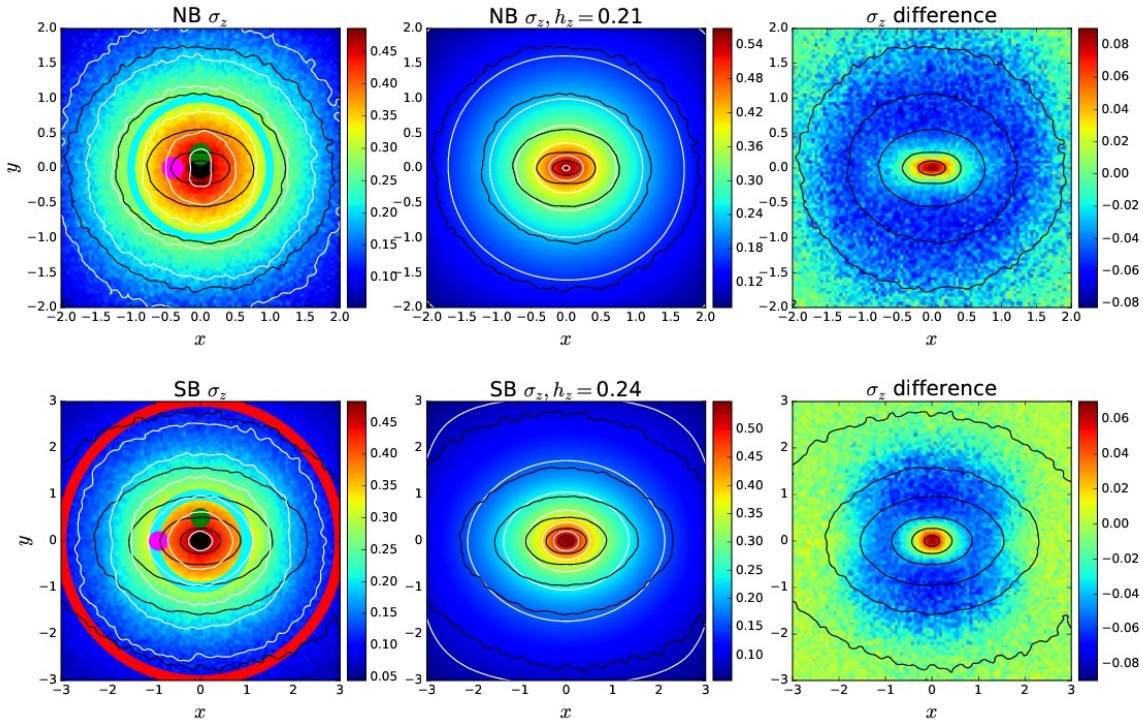

FIG. 15.— Numerically calculated σ_z using different vertical density distributions and their σ_z difference (right) maps. Based on Eqn. 4, the σ_z maps in the left panels are calculated using the original 3D density distributions from the NB (top) and SB (bottom) simulations. In the middle panels, without changing the surface density, we recalculate the σ_z maps by using a vertically exponential profile with a constant scaleheight. The constant scaleheights are set to the linear-fitting of the vertical density distributions of the NB ($h_z = 0.21$) and SB ($h_z = 0.24$) outer disks (Fig. 16), respectively. The right panels show the σ_z difference between the σ_z calculated using the original density and that using a vertically exponential density distribution. The smoothed surface density and σ_z contours are overlaid in black and white, respectively. In the left panels, the painted dots and annuli mark the regions we use to average the vertical density profiles in Fig. 16. In the NB model the red annulus at $R = 3.0$ is beyond the boundary of the image in the NB model, thus not shown here.

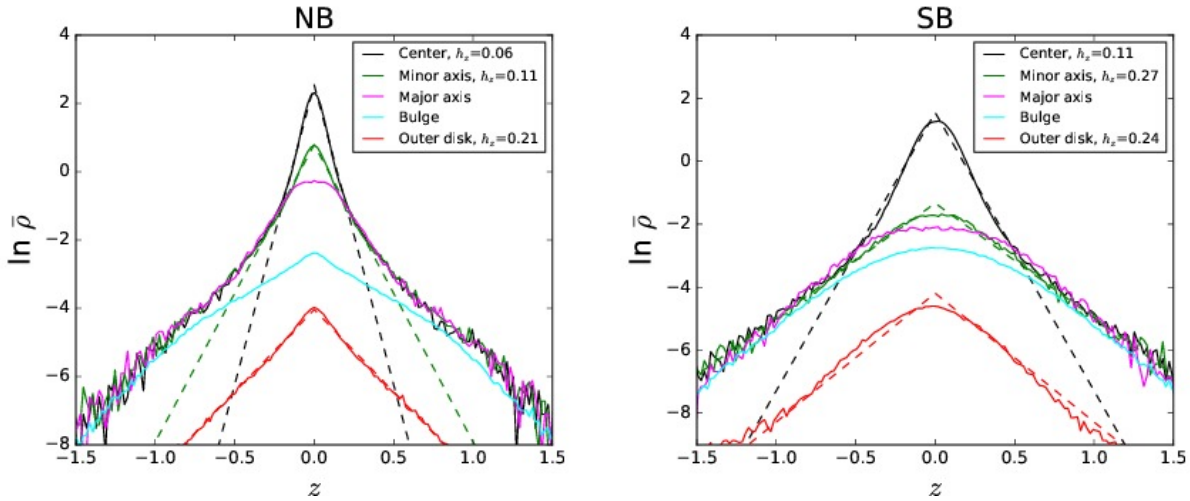

FIG. 16.— Average density ($\ln\bar{\rho}$) profiles of the NB (left) and the SB (right) models along the z direction. The profiles correspond to the vertical density distributions of the center (black), minor (green), and major (magenta) axes of the bar, B/P bulge (cyan), and outer disk (red) regions. The average regions are marked with the filled dots and annuli in the same color in Fig. 15. The dashed profiles represent the extrapolated linear-fitting of the $\ln\bar{\rho}$ profiles at the outer disk (red) and the center (black) and minor axis (green) of the bar. The fitted scaleheights are given in the legend.

the solid profiles using the same color. The dashed profiles represent the extrapolated linear-fitting of the $\ln\bar{\rho}$ profiles at each region. In the bar regions we only fit the region close to the mid-plane where the bar should dominate (for the NB $z \in [-0.3, 0.3]$, while for the SB $z \in [-0.5, 0.5]$). The density profiles on the major axis of the bar (magenta) and the B/P bulge (cyan) cannot be fitted by a linear relation. The fitted scaleheight values at each region are given in the legend. The nuclear bar of the NB model ($h_z = 0.11$ at the minor axis area) is vertically thinner than the host disk ($h_z = 0.21$), which agrees well with the analytical expectation for generating σ_z-humps+hollows. In contrast, the bar of the SB model is as thick as the disk, except for its very central region; thus it exhibits no σ_z-humps+hollows.

We calculate the σ_z difference using the same approach as in Sections 3.4 and 4. In the left panels of Fig. 15 we show the numerically calculated σ_z using the original 3D density distributions of the NB and SB models. In the middle panels σ_z is recalculated using the vertically exponential profiles with a constant scaleheight. The scaleheights used here are set to the linear-fitting results of the outer disks (NB $h_z = 0.21$; SB $h_z = 0.24$). Then the σ_z difference maps (the right panels) are obtained by subtracting the σ_z maps in the left panels from those in the middle panels. In this case, the non-zero σ_z difference represents the difference of vertical thickness from the outer disk. The σ_z difference is roughly equal to zero in the outer disk. In the NB model the σ_z difference is qualitatively consistent with the bar+disk+bulge model (Fig. 13). In the thin bar region the σ_z difference is positive at $\sim 10 - 20\%$ level, while in the thick B/P bulge region it turns to be negative ($\sim 15 - 30\%$ level). As visually confirmed from the edge-on view, the NB model hosts a nearly boxy bulge of radius $R \sim 1.5$. The negative σ_z difference traces the face-on morphology of such a boxy bulge. In the bottom-right panel, the B/P bulge of the SB model should correspond to the peanut-shaped negative region ($\sim 25\%$ level) in the σ_z difference map. A positive σ_z difference only appears at the very central region (marked with the filled black dot in Fig. 15) where $\bar{\rho}$ is peaked around the mid-plane.

In conclusion, the σ_z difference seems to be a good kinematic diagnostic for the stellar components having different thickness, e.g. thick bulges and thin bars. It may shed new light on the 3D geometry of bars and bulges in the face-on views of barred galaxies. It is worth emphasizing that, for real galaxies, h_z is generally estimated either from the empirical relation in de Grijs (1998) or the observed σ_z in the outer disk by assuming a reasonable mass-to-light ratio. In practice, the estimation of h_z still has a large uncertainty, and the mass-to-light ratio is not constant. This may cause large errors in the estimation of surface density. The practicality of this method will be tested in future work.

6. SUMMARY

By applying the vertical Jeans equation to a group of well-designed bar+disk(+bulge) models, we have systematically investigated the σ_z properties of barred galaxies from a purely dynamical point of view. The main conclusions can be summarized as:

(1) Bars can dynamically induce significant non-axisymmetric σ_z features, either σ_z-humps+hollows or oval σ_z contours aligned with bars. The properties of σ_z features are tightly related with the properties of bars, i.e., mass, length, ellipticity, and thickness. Generally, thick or long bar are more likely to generate oval σ_z contours aligned with bars.

(2) We found that vertically thin bars can not only reduce σ_z along the major axis of bars but also enhance σ_z along the minor axis, thus generating σ_z-humps+hollows. Such σ_z-humps+hollows can explain the σ-humps+hollows appearing in the kinematic observations of double-barred galaxies.

(3) As a dynamical response of stars to the potential of bars, the amplitude of σ_z-humps is proportional to the mass and ellipticity of bars, while it is almost independent of the bar thickness. σ_z-humps are mainly present in host disks, thus extending beyond bars. A thin bar mainly reduces σ_z in the bar region, thus generating σ_z-hollows.

(4) We showed that σ_z-humps+hollows are preferentially found in galaxies harboring a short bar, e.g. inner bars of double-barred galaxies and single nuclear bars. σ-humps+hollows have been commonly observed in double-barred galaxies, while their frequency in nuclear-barred galaxies is still unclear. In long bar cases σ_z-humps+hollowsare less frequent, possibly because volume expansion makes bar potential shallower.

(5) Using the bar+disk+bulge models, we show that the primary effect of a thick bulge is to make the σ_z-humps weaker by enhancing the central σ_z. Thus σ-humps+hollows should not be explained by the contrast of dynamically cold bars and hot bulges as proposed in previous analysis.

In IFU observations, an increasing number of σ-humps+hollows features have been identified in nearby S2Bs (de Lorenzo-Cáceres et al. 2008, 2013; Du et al. 2016). Du et al. (2016) presented self-consistent S2B simulations which match the kinematic observations of S2Bs. In this paper, we demonstrate that the existence of a vertically thin bar in the nuclear-barred simulation (NB) generates such σ-humps+hollows in small-scale (nuclear) bars. The interaction of multiple bars should play a minor role in generating σ-humps+hollows. The ubiquitous presence of σ-humps+hollows in S2Bs indicates that inner bars are vertically thin structures. Thus it suggests that inner bars are either not prone to thickening or they are younger structures formed in dynamically cold nuclear disks. However, the detailed stellar population analysis of S2Bs showed that inner bars are not young structures (de Lorenzo-Cáceres et al. 2012, 2013). In our simulations vertically thin bars also last for more than 5Gyr. Thus we propose that inner bars are weakly thickened after forming in initial nuclear disks.

As embedded in galactic central regions, the vertical thickness of bars is rarely measured in real galaxies. In low-inclination cases, it is also very difficult to identify the morphology of bulges. An implication of this work is that σ_z may trace the stellar components having different thickness, e.g. thin bars and thick bulges. It may

provide a novel perspective on the 3D geometry of bars and bulges from IFU surveys for nearly face-on galaxies.

M.D. thanks the Jeremiah Horrocks Institute of the University of Central Lancashire for their hospitality during a three month visit while this paper was in progress. M.D. thanks Adriana de Lorenzo-Cáceres for constructive comments on the manuscript. The research presented here is partially supported by the 973 Program of China under grant no. 2014CB845700, by the National Natural Science Foundation of China under grant nos.11333003, 11322326, and by the Strategic Priority Research Program "The Emergence of Cosmological Structures" (no. XDB09000000) of the Chinese Academy of Sciences. We acknowledge support from a *Newton Advanced Fellowship* #NA150272 awarded by the Royal Society and the Newton Fund. This work made use of the facilities of the Center for High Performance Computing at Shanghai Astronomical Observatory. V.P.D. is supported by STFC Consolidated grant # ST/J001341/1. V.P.D. was also partially supported by the Chinese Academy of Sciences President's International Fellowship Initiative Grant (No. 2015VMB004).

REFERENCES

Angus, R., Aigrain, S., Foreman-Mackey, D., & McQuillan, A. 2015, MNRAS, 450, 1787
Athanassoula, E. 2003, MNRAS, 341, 1179
Athanassoula, E., Machado, R. E. G., & Rodionov, S. A. 2013, MNRAS, 429, 1949
Athanassoula, E., & Sellwood, J. A. 1986a, MNRAS, 221, 213
—. 1986b, MNRAS, 221, 213
Bershady, M. A., Martinsson, T. P. K., Verheijen, M. A. W., et al. 2011, ApJ, 739, L47
Bershady, M. A., Verheijen, M. A. W., Swaters, R. A., et al. 2010, ApJ, 716, 198
Binney, J., & Merrifield, M. 1998, Galactic Astronomy
Binney, J., & Tremaine, S. 2008, Galactic Dynamics: Second Edition (Princeton University Press)
Bizyaev, D. V., Kautsch, S. J., Mosenkov, A. V., et al. 2014, ApJ, 787, 24
Bournaud, F., & Combes, F. 2002, A&A, 392, 83
Budiardja, R. D., & Cardall, C. Y. 2011, Computer Physics Communications, 182, 2265
Bundy, K., Bershady, M. A., Law, D. R., et al. 2015, ApJ, 798, 7
Bureau, M., & Athanassoula, E. 2005, ApJ, 626, 159
Bureau, M., & Freeman, K. C. 1999, AJ, 118, 126
Buta, R., & Block, D. L. 2001, ApJ, 550, 243
Buta, R., & Combes, F. 1996, Fund. Cosmic Phys., 17, 95
Buta, R., & Crocker, D. A. 1993, AJ, 105, 1344
Cappellari, M. 2016, ArXiv e-prints, arXiv:1602.04267
Cappellari, M., Emsellem, E., Bacon, R., et al. 2007, MNRAS, 379, 418
Cappellari, M., Emsellem, E., Krajnović, D., et al. 2011, MNRAS, 413, 813
Chapelon, S., Contini, T., & Davoust, E. 1999, A&A, 345, 81
Corsini, E. M., Debattista, V. P., & Aguerri, J. A. L. 2003, ApJ, 599, L29
de Grijs, R. 1998, MNRAS, 299, 595
de Jong, R. S. 1996, A&A, 313, 45
de Lorenzo-Cáceres, A., Falcón-Barroso, J., & Vazdekis, A. 2013, MNRAS, 431, 2397
de Lorenzo-Cáceres, A., Falcón-Barroso, J., Vazdekis, A., & Martínez-Valpuesta, I. 2008, ApJ, 684, L83
de Lorenzo-Cáceres, A., Vazdekis, A., Aguerri, J. A. L., Corsini, E. M., & Debattista, V. P. 2012, MNRAS, 420, 1092
de Vaucouleurs, G., de Vaucouleurs, A., Corwin, Jr., H. G., et al. 1991, Third Reference Catalogue of Bright Galaxies. Volume I: Explanations and references. Volume II: Data for galaxies between 0^h and 12^h. Volume III: Data for galaxies between 12^h and 24^h.
de Zeeuw, P. T., Bureau, M., Emsellem, E., et al. 2002, MNRAS, 329, 513
Debattista, V. P., Carollo, C. M., Mayer, L., & Moore, B. 2005, ApJ, 628, 678
Debattista, V. P., Mayer, L., Carollo, C. M., et al. 2006, ApJ, 645, 209
Debattista, V. P., & Sellwood, J. A. 1998, ApJ, 493, L5
—. 2000, ApJ, 543, 704
Díaz-García, S., Salo, H., Laurikainen, E., & Herrera-Endoqui, M. 2016, A&A, 587, A160
Du, M., Debattista, V. P., Shen, J., & Cappellari, M. 2016, ApJ, 828, 14
Du, M., Shen, J., & Debattista, V. P. 2015, ApJ, 804, 139
Elmegreen, B. G., & Elmegreen, D. M. 1985, ApJ, 288, 438
Emsellem, E., Renaud, F., Bournaud, F., et al. 2015, MNRAS, 446, 2468
Erwin, P. 2004, A&A, 415, 941
—. 2005, MNRAS, 364, 283
Erwin, P., & Sparke, L. S. 2002, AJ, 124, 65
Eskridge, P. B., Frogel, J. A., Pogge, R. W., et al. 2000, AJ, 119, 536
Fathi, K., Allen, M., Boch, T., Hatziminaoglou, E., & Peletier, R. F. 2010, MNRAS, 406, 1595
Ferrers, N. M. 1877, Q. J. Pure Appl. Math., 14
Friedli, D., & Martinet, L. 1993, A&A, 277, 27
Gadotti, D. A., & de Souza, R. E. 2006, ApJS, 163, 270
García-Burillo, S., Combes, F., Schinnerer, E., Boone, F., & Hunt, L. K. 2005, A&A, 441, 1011
Graham, A. W., & de Blok, W. J. G. 2001, ApJ, 556, 177
Harsoula, M., & Kalapotharakos, C. 2009, MNRAS, 394, 1605
Hohl, F. 1971, ApJ, 168, 343
Hopkins, P. F., & Quataert, E. 2010, MNRAS, 407, 1529
Iannuzzi, F., & Athanassoula, E. 2015, MNRAS, 450, 2514
Jeans, J. H. 1922, MNRAS, 82, 132
Kim, T., Gadotti, D. A., Athanassoula, E., et al. 2016, MNRAS, 462, 3430
Kim, W.-T., Seo, W.-Y., & Kim, Y. 2012, ApJ, 758, 14
Knapen, J. H., Shlosman, I., & Peletier, R. F. 2000, ApJ, 529, 93
Kormendy, J. 2013, Secular Evolution in Disk Galaxies, ed. J. Falcón-Barroso & J. H. Knapen, 1
Kormendy, J., & Kennicutt, Jr., R. C. 2004, ARA&A, 42, 603
Krajnović, D., Emsellem, E., Cappellari, M., et al. 2011, MNRAS, 414, 2923
Kuijken, K., & Merrifield, M. R. 1995, ApJ, 443, L13
Laine, S., Shlosman, I., Knapen, J. H., & Peletier, R. F. 2002, ApJ, 567, 97
Laurikainen, E., & Salo, H. 2002, MNRAS, 337, 1118
Laurikainen, E., Salo, H., & Buta, R. 2004a, ApJ, 607, 103
—. 2005, MNRAS, 362, 1319
Laurikainen, E., Salo, H., Buta, R., & Vasylyev, S. 2004b, MNRAS, 355, 1251
Laurikainen, E., Salo, H., & Rautiainen, P. 2002, MNRAS, 331, 880
Li, Z., Shen, J., & Kim, W.-T. 2015, ApJ, 806, 150
Maciejewski, W. 2004a, MNRAS, 354, 883
—. 2004b, MNRAS, 354, 892
Marinova, I., & Jogee, S. 2007, ApJ, 659, 1176
Martinet, L., & de Zeeuw, T. 1988, A&A, 206, 269
Martinsson, T. P. K., Verheijen, M. A. W., Westfall, K. B., et al. 2013a, A&A, 557, A131
—. 2013b, A&A, 557, A130
Menéndez-Delmestre, K., Sheth, K., Schinnerer, E., Jarrett, T. H., & Scoville, N. Z. 2007, ApJ, 657, 790
Merritt, D., & Sellwood, J. A. 1994, ApJ, 425, 551
Miller, R. H., Prendergast, K. H., & Quirk, W. J. 1970, ApJ, 161, 903
Miller, R. H., & Smith, B. F. 1979, ApJ, 227, 785
Mosenkov, A. V., Sotnikova, N. Y., Reshetnikov, V. P., Bizyaev, D. V., & Kautsch, S. J. 2015, MNRAS, 451, 2376
Nilson, P. 1973, Uppsala general catalogue of galaxies
Ostriker, J. P., & Peebles, P. J. E. 1973, ApJ, 186, 467
Patsis, P. A., Skokos, C., & Athanassoula, E. 2002, MNRAS, 337, 578
—. 2003, MNRAS, 342, 69

Pfenniger, D. 1984, A&A, 134, 373
Pfenniger, D., & Friedli, D. 1991, A&A, 252, 75
Raha, N., Sellwood, J. A., James, R. A., & Kahn, F. D. 1991, Nature, 352, 411
Salo, H., Laurikainen, E., Laine, J., et al. 2015, ApJS, 219, 4
Sánchez, S. F., Kennicutt, R. C., Gil de Paz, A., et al. 2012, A&A, 538, A8
Sánchez-Blázquez, P., Ocvirk, P., Gibson, B. K., Pérez, I., & Peletier, R. F. 2011, MNRAS, 415, 709
Schwarzkopf, U., & Dettmar, R.-J. 2000, A&A, 361, 451
Sellwood, J. A. 1980, A&A, 89, 296
—. 1981, A&A, 99, 362
—. 2014, ArXiv e-prints, arXiv:1406.6606
Sellwood, J. A., & Valluri, M. 1997, MNRAS, 287, 124
Sellwood, J. A., & Wilkinson, A. 1993, Reports on Progress in Physics, 56, 173
Shen, J., & Sellwood, J. A. 2004, ApJ, 604, 614
Sheth, K., Elmegreen, D. M., Elmegreen, B. G., et al. 2008, ApJ, 675, 1141
Shlosman, I., Begelman, M. C., & Frank, J. 1990, Nature, 345, 679
Shlosman, I., Frank, J., & Begelman, M. C. 1989, Nature, 338, 45
Skokos, C., Patsis, P. A., & Athanassoula, E. 2002a, MNRAS, 333, 847
—. 2002b, MNRAS, 333, 861
Valluri, M., Shen, J., Abbott, C., & Debattista, V. P. 2016, ApJ, 818, 141
Vauterin, P., & Dejonghe, H. 1997, MNRAS, 286, 812
Vega Beltrán, J. C., Pizzella, A., Corsini, E. M., et al. 2001, A&A, 374, 394
Villa-Vargas, J., Shlosman, I., & Heller, C. 2010, ApJ, 719, 1470
Whyte, L. F., Abraham, R. G., Merrifield, M. R., et al. 2002, MNRAS, 336, 1281